

Deep R-band photometry of the Chandra Deep Field South from the COMBO-17 survey

C. Wolf¹, K. Meisenheimer¹, S. Dye^{1,2}, M. Kleinheinrich¹, H.-W. Rix¹, and L. Wisotzki³

¹ Max-Planck-Institut für Astronomie, Königstuhl 17, D-69117 Heidelberg, Germany

² Astrophysics Group, Blackett Lab, Imperial College, Prince Consort Road, London, U.K.

³ Institut für Physik, Universität Potsdam, Am Neuen Palais 10, D-14469 Potsdam, Germany

Received / Accepted

Abstract. We report on deep multi-color imaging ($R_{5\sigma} = 26.0$) of the Chandra Deep Field South, obtained with the Wide Field Imager (WFI) at the MPG/ESO 2.2 m telescope on La Silla as part of the COMBO-17 survey. We include an overview of the COMBO-17 project and a detailed reduction scheme for WFI survey data. We discuss particular treatment necessary for accurate flatfielding of WFI images taken in the second half of 1999. As a result we present a catalog of 63501 objects in a field measuring $31'.5 \times 30'$ with astrometry and photometry. A sample of 35 variable objects is selected from two-epoch photometry. We try to give interpretations based on color, morphology and variation amplitude.

Key words. Techniques: image processing – Techniques: photometric – Surveys – Catalogs – quasars: general – X-rays: general

1. Introduction

Deep fields have become a favourite tool of observational cosmology, particularly in conjunction with the construction of multiwavelength datasets. Besides the ubiquitous Hubble Deep Fields, another illustrative example is the ROSAT Deep Survey in the Lockman Hole (Hasinger et al. 1998) and its optical follow-up by imaging and spectroscopy (e.g., Schmidt et al. 1998). However, full spectroscopic coverage is usually impossible to obtain, and the reconstruction of distances often has to rely on photometric redshift estimation. Despite major advances in this area, there is always a certain degree of degeneracy between object classes, such as different galaxy types, and their redshifts. Breaking this degeneracy is possible only by incorporating independent spectroscopic information, such as adding infrared colors or moving towards finer spectrophotometric resolution.

Wolf, Meisenheimer, & Röser (2001) and Wolf et al. (2001) demonstrated that the use of medium-band filters leads to a substantial gain in classification accuracy and discriminative power, as compared to simple broad-band photometry. In 1999 we initiated a new multicolor survey using the Wide Field Imager (WFI, Baade et al. 1998, 1999) at the MPG/ESO 2.2 m telescope on La Silla, Chile. The survey was designed to make full use of the capabilities offered by the WFI and at the same time exploit the experience collected in the course of earlier multicolor projects. By incorporating 17 different optical filters into our new survey (cf. Table 1), the COMBO-17 (*Classifying Objects by Medium-Band Observations in 17 filters*) project

goes a major step beyond the traditional multicolor approach. It permits confident spectral classification of objects with $I \lesssim 23$ into stars, galaxies, quasars, and the recognition of exotic objects, and it facilitates accurate subclassification, redshifts estimation, and SED reconstruction for galaxies and quasars. The survey area comprised four independent WFI fields (see Table 2), each of which was observed with the entire filter set. Overall objectives of COMBO-17 are:

- The galaxy catalog will be complete to $I < 23$ and contain $\sim 40\,000$ galaxies with accurate redshifts and spectral classification up to $z \simeq 1.3$, to be used to study the evolution of the galaxy luminosity function and clustering properties.
- The quasar sample will contain 500 to 1000 QSOs, with nearly uniform completeness over the redshift range $0.5 \lesssim z \lesssim 5$, well suited to trace the turnover in QSO evolution.
- Deep high-resolution R-band images permit morphological classification and gravitational lensing studies.

In this paper we focus on the “Chandra Deep Field South” (Giacconi et al. 2000) subject to a deep X-ray exposure by the Chandra satellite observatory and target of a wide range of multiwavelength studies from several groups. It is particularly worth noting that the COMBO-17 field of view contains the Chandra field entirely facilitating the efficient combination of optical and X-ray data. After a brief discussion of the COMBO-17 data reduction procedure, we present the first catalog of optically selected sources containing the Chandra field completely, down to R-band magnitudes of $R \lesssim 26$. This catalog will also be made publically available over the world-wide web.

Table 1. The COMBO-17 filter set with exposure times and 10- σ magnitude limits expected for point sources. The R -band observations have been performed in excellent seeing conditions ($0''.75$ PSF) on all four fields, but 25.2 mag is the 10 σ limit we obtained after convolving all frames to $1''.5$ effective PSF for obtaining accurate color indices. An independent R -band analysis could potentially go deeper.

$\lambda_{\text{cen}}/\text{fwhm}$ (nm)	Name	$t_{\text{exp}}/\text{sec}$	$m_{\text{lim},10\sigma}$
364/38	U	20000	23.5
456/99	B	7500	25.0
540/89	V	6000	24.5
652/162	R	20000	25.2
850/150	I	7500	23.0
420/30		10000	23.6
462/14		10000	23.5
485/31		5000	23.4
518/16		6000	23.3
571/25		4000	23.2
604/21		5000	23.1
646/27		4000	23.0
696/20		6000	22.8
753/18		7000	22.7
815/20		10000	22.6
856/14		18000	22.5
914/27		16000	22.4

Table 2. Positions and galactic reddening (Schlegel et al. 1998) for the COMBO-17 fields. All fields are observed with the Wide Field Imager at the MPG/ESO 2.2 m-telescope at La Silla observatory.

Field	α_{J2000}	δ_{J2000}	l_{gal}	b_{gal}	E_{B-V}
SGP	00 ^h 45 ^m 56 ^s	-29°35'15"	328°8	-87°3	0.02
Chandra	03 ^h 32 ^m 25 ^s	-27°48'50"	223°6	-54°5	0.01
A 901	09 ^h 56 ^m 17 ^s	-10°01'25"	248°0	+33°6	0.06
S 11	11 ^h 42 ^m 58 ^s	-01°42'50"	270°5	+56°8	0.02

2. The COMBO-17 observations

The project was granted a total of 47.5 observing nights within MPG time at the MPG/ESO 2.2-m telescope, between February 1999 and January 2001. Altogether, 35 nights were useably clear and had seeing below $1''.4$, our limit for survey exposures. Including all calibration exposures the total raw data volume of the COMBO-17 survey amounts to about 500 GBytes.

2.1. Imaging

The filter set employed by COMBO-17 is shown in Table 1. It comprises the five broad-band filters $UBVRI$ and 12 medium-band filters, which are rather uniformly spread across the wavelength range of the detector. While covering the range from 400 to 930 nm somewhat sparsely, we were able to pick filters such that they avoid strong night sky emission lines, thus going as deep as possible within a limited exposure time.

Table 3. Observing log for B , V and R exposures on the Chandra Deep Field South as part of the COMBO-17 survey.

Epoch (UT)	Band	Seeing	Exposure (sec)
1999, Oct 10	V	$\sim 1''.2$	$14 \times 600 + 3 \times 20$
1999, Oct 13	B	$\sim 1''.2$	$10 \times 500 + 3 \times 20$
1999, Oct 19	R	$\sim 0''.75$	25×420
1999, Oct 20	R	$\sim 0''.75$	$11 \times 420 + 1 \times 370$
2000, Feb 6	R	$\sim 0''.75$	$6 \times 500 + 2 \times 60$
2000, Feb 8	R	$\sim 0''.75$	$10 \times 500 + 1 \times 200 + 2 \times 60$

Here we discuss only data taken on the Chandra Deep Field South in the filters B , V and R (see Table 3 for a brief observing log). Our data encompass a total exposure time of 5000 sec in B and 8400 sec in V with seeing on the order of $\sim 1''.2$ and altogether 23700 sec in R with $\sim 0''.75$ mean PSF. Besides long exposures for efficient light gathering, we included short exposures for the photometry of brighter objects, in particular to avoid saturation of our brighter standard stars.

The long exposures followed a dither pattern with ten telescope pointings spread by $\Delta\alpha, \Delta\delta < \pm 72''$. This dither pattern is motivated by the intent to close the gaps in the CCD mosaic, but limited by the requirement of keeping field rotation at a minimum.

Twilight flatfields were obtained with offsets of $10''$ between consecutive exposures. Exposure times ranged between 0.5 and 100 seconds per frame (note that the WFI shutter design allows exposures as short as 0.1 seconds without causing significant spatial variations in the illumination across the CCD mosaic (Wackermann 1999)).

2.2. Standard stars

In order to achieve a homogeneous photometric calibration for all 17 WFI filter bands, we have established our own set of tertiary standard stars based on *spectrophotometric* observations. Two stars of spectral types G–F and magnitudes $B_J \simeq 16$ were selected in each COMBO-17 field, drawn from the Hamburg/ESO Survey database of digital objective prism spectra (Wisotzki et al. 2000). The spectrophotometric observations for the Chandra Deep Field South were conducted at La Silla on Oct 25, 1999, using the Danish 1.54 m telescope equipped with DFOSC. A wide ($5''$) slit was used for the COMBO-17 standards as well as for the external calibrator, in this case the HST standard HD 49798 (Bohlin & Lindler 1992). Two exposures of 45 min were taken of each star, one with the blue-sensitive grism 4 covering the range $\lambda = 3400\text{--}7400 \text{ \AA}$, and one with the red-sensitive grism 5 covering $\lambda > 5200 \text{ \AA}$.

The spectra were reduced by standard procedures and have a final signal-to-noise ratio of > 30 per pixel except very near to the low- and high-wavelength cutoffs. The agreement between spectra in the substantial overlap in wavelength between the two grisms is excellent, confirming that contamination from second order was negligible. The absolute spectrophotometric accuracy, estimated from comparing several spectra of the external calibrator HD 49798 obtained during the entire observing run, is better than 10 %.

3. The reduction pipeline

All procedures used for reduction are based on the MIDAS package and are routinely used at MPIA. The image processing and photometry pipeline have been developed specifically for dithered WFI survey images with participation by S. Dye, M. Kleinheinrich, K. Meisenheimer and C. Wolf in the years 1999 and 2000. This pipeline is installed as a MIDAS context file WFI and makes use of routines from the MIDAS context package MPIAPHOT developed by K. Meisenheimer and H.-J. Röser including some algorithms provided by H. Hippelein. The astrometry is based on the MIDAS context ASTROMET.

3.1. Image processing pipeline

The image processing pipeline is used for basic reduction from raw images to summed frames, and flatfield- and cosmic corrected individual frames. The reduction starts with a standard bias subtraction, followed by a non-linearity correction for four of the eight CCD chips in the mosaic (Baade 1999). The next step is the composition of a mosaiced frame with 8500×8500 pixels, into which the eight individual CCDs are inserted at optimal positions while the gaps and also CCD defects are set to zero by multiplying the image with a bad column and hot pixel mask. Since the mosaic contains engineering grade CCDs, there are many, even clustered bad columns.

Three CCDs are significantly rotated (up to $6'$) compared to the remaining five CCDs which are well aligned among each other. The former need to be rotated in order to ensure optimum object locations on the pixel grid of the mosaiced image. Image rotation involving a rebin operation does not preserve pixel flux values and produces diffusion of cosmic ray hits, hot pixels and bad columns. In order to avoid these effect, we simulate a rotation on the pixel grid by skewing the CCD images consecutively in their two axes. The skewing is done by cutting the image into the necessary number of slices, shifting all slices by one pixel with respect to the neighboring slice and subsequently inserting the result images into the large mosaic frame.

After a standard flatfield correction (details see following subsection) the positions of bright unsaturated objects are measured to establish coordinate transformations between all frames. This transformation is required for the cosmic correction and subsequent stacking of the cleaned frames. Since neither the cosmic correction nor the stacking operation uses any sub-pixel rebinning of the data but only operations on the given pixel grid, the transformation takes only translation with integer pixel values into account. An important factor is the rotation of the coordinate system introduced by the alpha offsets in the dither pattern. To account for this rotation, the full mosaic is cut into 4 by 4 subfields of roughly 2000×2000 pixels, within which the image rotation always accounts to less than a pixel dislocation. The transformations between all frames are therefore determined for each subfield individually based on about 50 to 100 stars per subfield and frame.

Cosmic correction is then performed by comparing the flux values of individual pixels among all frames. After scaling all frames to the same object flux level and background level, a

median image is calculated. When comparing frames with the median frame, outlier pixels are replaced by the median flux value and are flagged in a cosmic mask frame. Pixels with zero value are ignored since they mark places of no information. All cleaned subfields from the frames are stacked into a deep coadded image covering the area that is common to all frames, measuring $31.5 \times 30'$ in our case. The gaps and bad columns have become invisible since the stacking is performed via an averaging operation which only includes values above zero. The level of background and object flux in the coadded frame is finally adjusted to match the sum of all backgrounds and the sum of all object fluxes which go into the summed frame.

The coadded frame thus obtained is not optimal for photometry since the number of photons in each pixel depends on the local number of frames providing information. In fact, we use the deep coadded image only for object search and crude morphology as well as for visual inspection purposes. The photometry is instead performed on each individual frame and described in the next subsection. Objects are searched on the sum frame with SExtractor software (Bertin & Arnouts 1996) and positions, morphology, and the two magnitudes MAG-BEST (best guess) and MAG-ISO (isophotal) are extracted. We first search rather deep and then clean the list of found objects from those having more than 0.33 mag error in the SExtractor best-guess magnitude. We call the remaining list our *master list* for the Chandra field, which contains 63501 objects with positional information for our subsequent photometric analysis.

3.2. Special treatment of WFI flatfields from 1999

Standard flatfields are constructed by averaging several dusk flats. Distortions due to bright stars popping through the homogeneous twilight level are avoided by dithering the dusk flat exposures and employing a 3σ -clipping in the averaging procedure of those sequences. However, the flatfield correction of the October 1999 data requires special treatment due to the combination of two effects:

1. Between commissioning in January 1999 and the observations the CCD mosaic suffered from a surface contamination which was most severe near the outer edges of the mosaic. This led to a decrease in quantum efficiency which was most severe at short wavelength ($\lambda \lesssim 500$ nm) but extended out into the red. The contamination and its origin were removed in a servicing mission around Dec 1, 1999, when the CCD mosaic was baked and the culprit (some glue in the lower part of the WFI dewar) was replaced by a vacuum-proof component.
2. The original shutter end plate (made from oxidized aluminium) had to be replaced (in June 1999) by a plate made from Nylon to get a better shutter performance at low temperatures ($\lesssim 5^\circ\text{C}$). Nobody was aware, that the edges of the plate (running parallel to the optical axis) caused a largely increased amount of scattered light from sources outside of the field, despite black appearance. But this design fault could only be found, after problem (1) had been solved. A new shutter end plate with edges tilted away from the beam

was installed on the afternoon of Feb 4, 2000, in the middle of a COMBO-17 observing run.

However, in the period between June 1999 and January 2000, there is scattered background light in a ring subtending about $2'$ from the edges of the field of view and reading a level of a few percent. If the enhanced ring of (scattered) twilight level in the flatfields was treated as a true flatfield property, one would change the background in the science frames and corrupt the photometry of objects within a few arcminutes of the edge by several percent.

We were able to disentangle the effects of problems (1+2) by finding out, that multiplying the standard flatfield from October 1999 with a smoothed superflat derived from the October science frames leads to a very good agreement in the R-band photometry of both epochs (see also Fig. 9). Accordingly, we conclude that problem (1), the CCD contamination, is accounted for by standard flatfields, but superflats are needed for all science images taken in our October 1999 run to correct for problem (2).

3.3. Photometry and calibration

The photometric pipeline works in principle fully automatic on a set of reduced frames and generates a final calibrated object table with photometry on all available filters.

First, the object coordinates from the master list need to be projected onto each single frame. For this purpose, we determine the coordinate transformation of each individual frame with respect to the sum frame. Again, we cut the frame into 4 by 4 subfields of $\sim 2000 \times 2000$ pixels, and determine the transformation from up to 100 bright objects in each subfield, using the same procedures as above in the context of cosmic correction and stacking. This time the transformation solution takes translation, rotation and scaling in two independent axes into account. The full linear transformation is applied to all objects within a subfield of the single frame. From a large sample of bright stars on the whole frame the rms positional error and the PSF is determined.

Second, on each individual frame count rates are measured within an aperture around the projected object coordinate. COMBO-17 is a spectrophotometric survey, where color indices are the prime observables entering a process of classification and redshift estimation later. Therefore, it is necessary to choose an optimum way to measure these indices. For ground-based observations it is important to avoid that variable observing conditions introduce offsets between bands when the observations are taken sequentially. Variable seeing, e.g. might influence the flux measurement of star-like and extended objects in a different way.

This requires to assess the seeing point spread function on every dataset very carefully. Then, we essentially convolve each image to a common *effective* point spread function and measure the central surface brightness of each object (Röser & Meisenheimer 1991). This has the disadvantage that the spatial resolution (i.e. the minimum separation of objects neighboring each other) is limited by the data with the poorest seeing. For the context of this paper we convolve all frames to a common

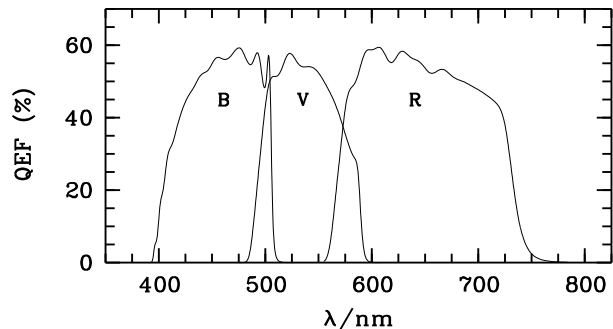


Fig. 1. Total system efficiencies for the WFI filters *B*, *V* and *R* (including telescope, instrument and detector).

seeing of $1''.5$, which means that the *R*-band images taken in $0''.75$ seeing lose some depth, especially for point sources.

The flux calibration is performed by identifying our spectrophotometric standard stars and convolving their spectra with the total system efficiency in the given filter (see Fig. 1). We then know the physical photon flux we have to assign to them, and establish the flux scale for all objects. Eventually, the measurements of all frames taken with a given filter are combined. If the standard stars of a frame are saturated, the fluxes are scaled via the other frames by using a few hundred well measured objects from each frame as internal standards.

The individual fluxes are averaged into a final flux for each object with the error being derived from the scatter of the individual measurements. This way, the error does not only take photon noise into account, but further sources of error, such as imperfect flatfielding and uncorrected CCD artifacts. However, we prevent chance coincidences of count rates from pretending unreasonably low errors by using the photon noise as a lower limit (Meisenheimer et al., in preparation). As a last organizational step we combine the flux values from all filters into one catalog and check the quality of photometry and calibration. Once enough filters are available, a multi-color classification and redshift estimation can be applied to the catalog.

3.4. Astrometry

The astrometric calibration was done in two main steps: First, the astrometric standard set by the PPM stars (Röser & Bastian 1991) was used to determine an astronomical coordinate system on the DSS-2 Schmidt plate containing the Chandra field. Then bright stars common to the DSS-2 plate and our CCD sum frame have known coordinates and are used to establish the coordinate system on the CCD image. All coordinates cited are measured in this last coordinate system (see Fig. 2).

As a first step, we retrieved a $30' \times 30'$ FITS image of the red sensitive emulsion of the DSS-2¹ survey from the ESO

¹ The “Second Epoch Survey” of the southern sky was produced by the Anglo-Australian Observatory (AAO) using the UK Schmidt Telescope. Plates from this survey have been digitized and compressed by the ST ScI. The digitized images are copyright (c) 1993-1995 by the Anglo-Australian Telescope Board, and are distributed herein by agreement. All Rights Reserved. Produced under Contract No. NAS 5-26555 with the National Aeronautics and Space Administration.

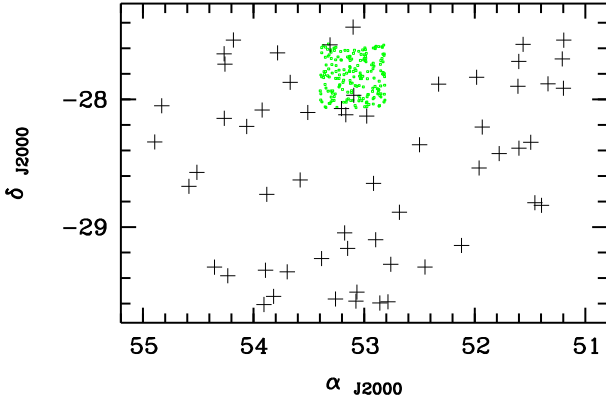


Fig. 2. Positions of 58 PPM stars (crosses) and ~ 200 bright stars from the master list of our field (grey dots). The field lies near the Northern end of the DSS-2 plate, which explains why only few PPM stars are available on the same plate to the North of the field.

website. Then we selected PPM stars fainter than 9.5 mag and located within a circle of 2° radius around the center of the field at $\alpha = 3^h 32^m 25^s$ and $\delta = -27^\circ 48' 50''$ (J2000.0), which have to be on the same red-sensitive emulsion plate of the DSS-2 survey (plate ID = A21D, label = OR17388). We also retrieved a $1' \times 1'$ FITS image for each of these PPM stars from DSS-2. On the FITS images we recovered the original plate positions of the PPM stars. Then we derived the coordinate system on the plate with MIDAS astrometry routines and accounted for distortion by using a cubic plate solution an internal accuracy of $\sigma \approx 0''.25$.

For the second step, we select ~ 200 bright stars ($17 < R < 19.5$) from the master list, which are unsaturated on the CCD image. The positions of these stars are measured on the DSS image and their α/δ -values are calculated in the coordinate system of the DSS plate. These positions are now used as astrometric standards for deriving a cubic plate solution on the CCD frame, again using MIDAS astrometry software. Having the coordinate system defined on the CCD frame, we now calculate final positions for the entire catalog.

The internal accuracy of the final CCD astrometry is $\sigma \approx 0''.14$, a rather large value compared to $0''.10$ which should be feasible for non-mosaic cameras. The lower accuracy results from the fact that the positions are measured on a mosaiced coadded frame created without sub-pixel operations. In fact, the coadded frame has large areas where the image data always come from the same CCD chip of the mosaic, but has also regions where data from neighboring CCDs are stacked into the same pixel of the sum frame since we explicitly dithered across the mosaic gaps. In the latter regions, the object positions are less accurate than in the former areas.

4. The catalog and initial results

The object catalog derived from the observations presented contains positions and *BVR* photometry of 63501 objects selected in *R* within a field of $31.5 \times 30'$ size. The depth and the seeing quality of our *R*-band imaging makes this cat-

Table 4. Content of the object catalog made available at CDS.

Label	Explanation
Seq	Sequential number
RA	Right ascension (J2000), internal accuracy $\pm 0''.15$
DE	Declination (J2000), internal accuracy $\pm 0''.15$
Class	SExtractor stellarity.
Rmag	Aperture magnitude, scaled to total flux for stars
e-Rmag	Mean error (sigma) of Rmag
Rmag-best	SExtractor magnitude, best guess, scaled to match Rmag for stars at $R=18..20$
Rmag-iso	SExtractor magnitude, isophotal, scaled to match Rmag for stars at $R=18..20$
MajAxis	Major axis from SExtractor
MinAxis	Minor axis from SExtractor

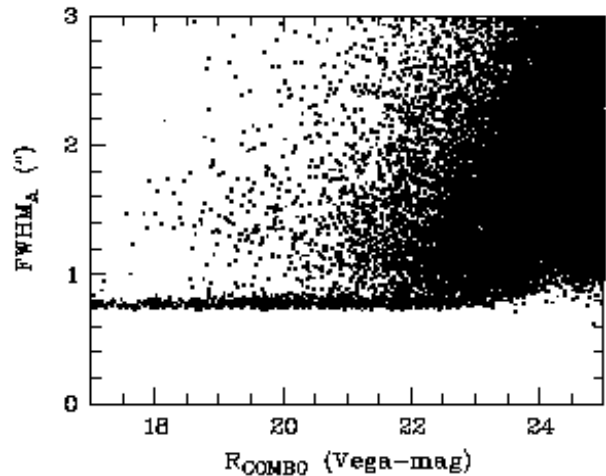


Fig. 3. Distribution of FWHM values for the major axis versus *R* magnitude. This shows that star-galaxy separation is feasible at $R < 23$.

alog potentially very useful for the identification of X-ray sources and other purposes. In order to provide the scientific community with part of our data, we have made the catalog with positions and *R*-band photometry publicly available at Centre de Données astronomiques de Strasbourg (CDS, <http://cdsweb.u-strasbg.fr/>). Table 4 lists the information contained in the public table. In the following two subsections we discuss data quality issues that could be relevant for making best use of the catalog. In Sect. 4.3 we present a first sample of variable objects identified from the two epochs of *R*-band observations.

4.1. Morphology and photometry

As morphological parameters, the catalog includes the full width half maximum (FWHM) measurements for major and minor axis determined by SExtractor together with a “stellarity parameter”. The stellarity seems to consider many objects point sources which appear still extended based on their FWHM values. Fig. 3 plots the FWHM of the major axis versus our *R*-band magnitude. While the point sources are clearly distinguishable at $R < 23$, a reliable separation seems out of

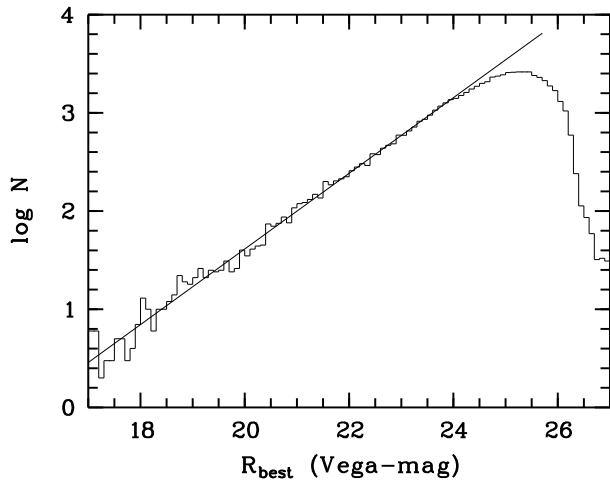


Fig. 4. Number counts histogram of all objects excluding ~ 1050 stellar objects with $R < 24$. The histogram is based on the SExtractor magnitude MAG-BEST derived on the deep sum frame from October 1999. At $R > 24$ no star-galaxy separation is available, but the remaining stars in the sample should not contribute a significant fraction. Note, that this plot contains 62457 objects and shows their counts in bins of 0^m1 . A line with a slope of 0.835 was fitted to the data at $R < 24$.

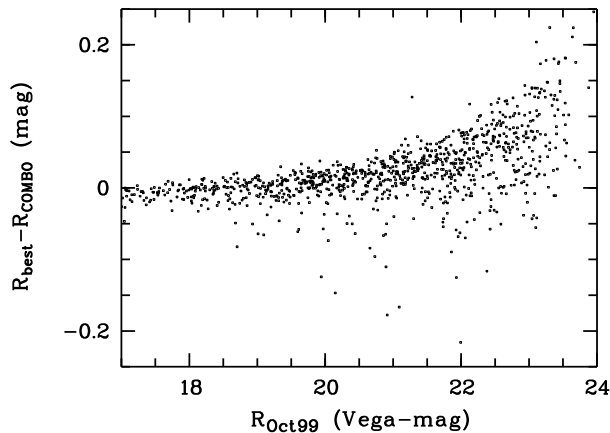


Fig. 5. Difference between the SExtractor magnitude MAG-BEST derived on the deep sum frame and the COMBO-17 magnitude from October 1999, here shown only for stellar objects. MAG-BEST has been calibrated to match the COMBO-17 photometry for stars of $R = 18 \dots 20$. Ideally, the sample should scatter around zero everywhere, but apparently there are deviations towards fainter magnitudes for which we do not know the reason.

reach for fainter sources. For all purposes of this paper we defined point sources as objects with $R < 24$ and a major axis of $< 0''.85$ FWHM.

The photometric data quality differs for point sources and extended sources. Our photometry is a seeing-adaptive central surface brightness measurement giving accurate fluxes for point sources while underestimating the total flux of extended sources. Since our photometry is performed on the individual frames in an optimal fashion, it reaches deeper magnitudes and estimates the errors more accurately than the SExtractor pho-

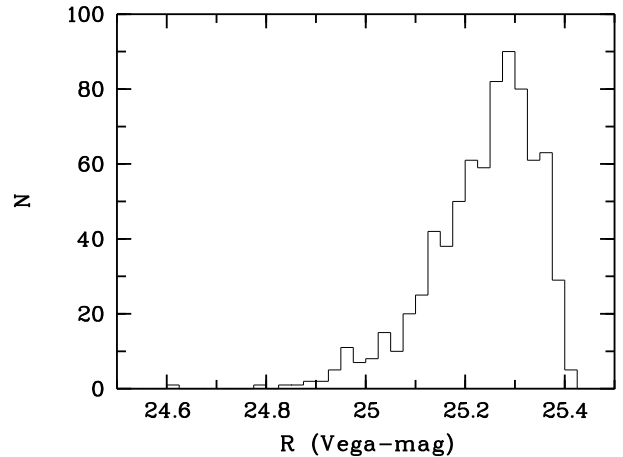


Fig. 7. R-band histogram of objects with errors of $0^m099 \dots 0^m101$. From this distribution we read the 10σ limiting magnitude as the median at $R = 25^m25$. We have smoothed all images to an effective PSF of $1''.5$ in order to match the photometry from all bands into accurate colors.

tometry we have derived from the coadded frame. In contrast to SExtractor, our photometry does not provide an aperture correction for extended sources. For the purpose of total magnitudes, we included the SExtractor magnitudes MAG-BEST and MAG-ISO calibrated by matching them with our R -band photometry of stars with $R = 18 \dots 20$.

Fig. 4 shows a number counts histogram of the SExtractor magnitude MAG-BEST excluding the ~ 1050 point sources identified at $R < 24$. While the counts agree quantitatively with number counts published earlier by other groups, a detailed discussion will be presented in an independent publication.

In Fig. 5 we compare our R -band magnitude from the October 1999 observations with the SExtractor MAG-BEST measured on the October 1999 sum frame. For point sources these two measurements should ideally agree, especially since we calibrated MAG-BEST to match our R -band magnitude of stars with $R = 18 \dots 20$. However, we observe that MAG-BEST seems to slightly underestimate the flux of faint stars by about 5% to 10% at $R \sim 23$ and probably rises to larger deviations at fainter levels. We do not know the reason for this difference, but it might be related to the quality of the morphology measurement which obviously degrades towards faint magnitudes (see below). While MAG-BEST is sensitive to morphology, our magnitude ignores the source extent and should therefore be more accurate for true point sources.

Fig. 6 shows the photometric errors versus magnitudes of all objects we measured at less than 0^m1 error. The photon noise limit can be seen as a sharp parabolic edge to the right of the object clouds. We use magnitude histograms of objects with errors between 0^m099 and 0^m101 to assess a representative $10\text{-}\sigma$ magnitude limit. In Fig. 7 we can see that all R -band images combined reach $R_{\text{lim},10\sigma} = 25.25$, which is precisely $R_{\text{lim},5\sigma} = 26.00$. We note, that we have not exploited the depth of these images ($0''.75$ PSF) by convolving them all to a common worst survey seeing of $1''.5$.

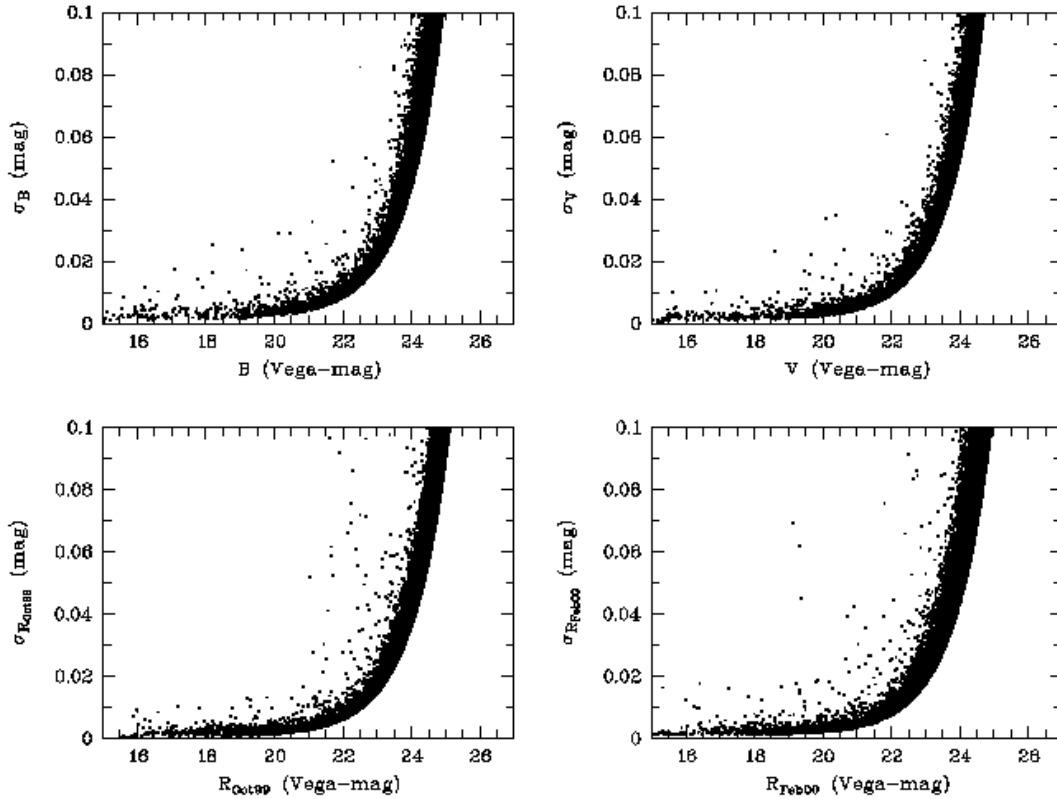


Fig. 6. Errors versus magnitudes for all objects with errors below 0^m1 observed in the WFI filters B, V and R (two epochs).

4.2. Calibration quality

We check the flux calibration by comparing measured colors of stellar objects with those predicted by synthetic photometry. We convolved the Pickles (1998) library of stellar spectra with the total efficiency curves of our filters and plotted their $B - V$ and $V - R$ colors as black dots in Fig. 8. Our own point sources are overplotted as grey dots and agree with the expected colors without any further correction. Shown are photon count color indices in units of CDmag that were defined by Wolf et al. (2001). As a physical magnitude definition besides ABmag and STmag the CDmag is

$$CDmag = -2.5 \log F_{\text{phot}} + 20^m01 \quad (1)$$

with F_{phot} in $\gamma \text{ m}^{-2} \text{ s}^{-1} \text{ nm}^{-1}$,

and matches the common magnitude zeropoint of (astronomical) Vega-mag, ABmag and STmag at $\lambda_0 = 548 \text{ nm}$.

We note that most stars observed in our field belong to the halo population, while most stars in the Pickles library are nearby stars from the disk population. The populations form two arms that are separated for G/K stars ($B - V_{CD} \approx 0.3 \dots 0.6$). Since the population densities on the two arms differ between data and library, a wrong impression of an apparent calibration shift is raised. We also note a few blue objects off the main sequence, which are most likely quasars passing our purely morphological selection.

4.3. A first set of variable objects

For variability studies we calculated a magnitude change between the two epochs October 1999 and February 2000 and a related error as:

$$\Delta R = R_{\text{Feb00}} - R_{\text{Oct99}} - 0^m009, \quad (2)$$

and

$$\sigma_{\Delta R} = \sqrt{\sigma_{R_{\text{Oct99}}}^2 + \sigma_{R_{\text{Feb00}}}^2}. \quad (3)$$

The magnitude difference has in fact been adjusted by 0^m009 corresponding to 0.9% change in flux calibration of one epoch. Fig. 9 shows the magnitude difference of all objects with $R < 25$ versus the combined R -magnitude. The distribution underlines that the photometric errors are realistic and the photometry is essentially consistent among the two epochs.

We selected a sample of variable objects using the following criteria:

1. faint cutoff: at least one detection must have $R < 24$
2. absolute variability threshold: $\Delta R > 0.1$
3. variability significance threshold: $\Delta R / \sigma_{\Delta R} > 5$

This way 55 entries are selected in the catalog which were made subject to visual inspection on the sum frames of the two epochs. We eliminated 20 faint objects from the sample which were affected by scattered light or diffraction spikes of 9^{th} magnitude stars. We have confidence in the variability of the remaining 35 objects and list their positions and original photometry from the two epochs in Table 5. The number of variable objects increases strongly with fainter magnitude but faintwards

Table 5. A first sample of variable objects drawn from R -band photometry of two epochs. While most objects are likely to be quasars at $z < 3$, we comment on exceptions. Some objects appear slightly extended (ext.), which would most likely be resolved host galaxies of either Supernovae or Seyfert nuclei (Sy).

no	object name	α_{J2000}	δ_{J2000}	R_{Oct99}	R_{Feb00}	comment
1	COMBO-0332271-280336	03 ^h 32 ^m 27 ^s .071	-28°03′35″.85	23.094 ± 0.018	23.281 ± 0.029	F2-F5 star colors
2	COMBO-0332323-280328	03 ^h 32 ^m 32 ^s .286	-28°03′28″.30	21.281 ± 0.004	21.395 ± 0.005	
3	COMBO-0331278-280156	03 ^h 31 ^m 27 ^s .775	-28°01′55″.69	23.018 ± 0.024	22.847 ± 0.019	Sy or $z \approx 4$ -QSO
4	COMBO-0331362-280149	03 ^h 31 ^m 36 ^s .248	-28°01′49″.43	22.195 ± 0.008	21.992 ± 0.012	
5	COMBO-0332302-280020	03 ^h 32 ^m 30 ^s .205	-28°00′20″.14	21.746 ± 0.006	21.919 ± 0.009	
6	COMBO-0333149-275749	03 ^h 33 ^m 14 ^s .852	-27°57′48″.98	23.408 ± 0.022	23.032 ± 0.022	
7	COMBO-0331208-275649	03 ^h 31 ^m 20 ^s .765	-27°56′48″.89	20.657 ± 0.003	20.782 ± 0.004	F0 star colors
8	COMBO-0332041-275627	03 ^h 32 ^m 04 ^s .149	-27°56′26″.58	22.966 ± 0.016	22.762 ± 0.021	ext.
9	COMBO-0332226-275623	03 ^h 32 ^m 22 ^s .605	-27°56′22″.70	22.277 ± 0.010	22.562 ± 0.015	ext., SN candidate
10	COMBO-0333053-275409	03 ^h 33 ^m 05 ^s .327	-27°54′09″.18	21.515 ± 0.005	21.390 ± 0.011	ext.
11	COMBO-0333042-275103	03 ^h 33 ^m 04 ^s .223	-27°51′02″.79	22.270 ± 0.011	22.401 ± 0.014	M star colors
12	COMBO-0331525-275028	03 ^h 31 ^m 52 ^s .494	-27°50′27″.57	22.394 ± 0.010	22.561 ± 0.014	ext., Sy or $z \approx 4$ -QSO
13	COMBO-0333104-274945	03 ^h 33 ^m 10 ^s .405	-27°49′44″.73	23.136 ± 0.019	21.997 ± 0.008	
14	COMBO-0332433-274914	03 ^h 32 ^m 43 ^s .252	-27°49′14″.16	22.225 ± 0.008	22.746 ± 0.019	
15	COMBO-0333328-274908	03 ^h 33 ^m 32 ^s .753	-27°49′07″.73	21.440 ± 0.007	21.584 ± 0.008	
16	COMBO-0333263-274831	03 ^h 33 ^m 26 ^s .305	-27°48′31″.03	22.890 ± 0.018	22.661 ± 0.023	
17	COMBO-0332087-274734	03 ^h 32 ^m 08 ^s .662	-27°47′34″.23	18.703 ± 0.001	18.853 ± 0.001	
18	COMBO-0332142-274647	03 ^h 32 ^m 14 ^s .243	-27°46′47″.45	23.409 ± 0.022	23.630 ± 0.031	ext.
19	COMBO-0333343-274621	03 ^h 33 ^m 34 ^s .335	-27°46′20″.80	23.262 ± 0.021	25.332 ± 0.185	SN candidate (red!)
20	COMBO-0332391-274602	03 ^h 32 ^m 39 ^s .095	-27°46′01″.79	20.634 ± 0.002	20.843 ± 0.003	
21	COMBO-0332300-274530	03 ^h 32 ^m 29 ^s .988	-27°45′29″.80	21.039 ± 0.003	21.196 ± 0.005	
22	COMBO-0333036-274519	03 ^h 33 ^m 03 ^s .634	-27°45′18″.64	22.769 ± 0.014	22.906 ± 0.020	
23	COMBO-0332302-274504	03 ^h 32 ^m 30 ^s .224	-27°45′04″.49	21.915 ± 0.007	22.035 ± 0.009	
24	COMBO-0332109-274415	03 ^h 32 ^m 10 ^s .918	-27°44′14″.67	22.286 ± 0.008	22.193 ± 0.010	
25	COMBO-0331533-274412	03 ^h 31 ^m 53 ^s .347	-27°44′12″.06	22.888 ± 0.017	22.568 ± 0.015	ext.
26	COMBO-0333358-274360	03 ^h 33 ^m 35 ^s .829	-27°43′59″.96	22.916 ± 0.015	23.091 ± 0.019	ext.
27	COMBO-0332591-274339	03 ^h 32 ^m 59 ^s .083	-27°43′39″.44	21.421 ± 0.004	21.328 ± 0.006	ext.
28	COMBO-0332004-274319	03 ^h 32 ^m 00 ^s .354	-27°43′19″.39	21.999 ± 0.006	22.162 ± 0.009	
29	COMBO-0331187-274121	03 ^h 31 ^m 18 ^s .703	-27°41′21″.31	21.927 ± 0.006	21.502 ± 0.007	
30	COMBO-0333289-274044	03 ^h 33 ^m 28 ^s .933	-27°40′43″.63	22.412 ± 0.009	22.684 ± 0.016	
31	COMBO-0332375-273960	03 ^h 32 ^m 37 ^s .452	-27°39′59″.99	22.521 ± 0.010	22.631 ± 0.014	
32	COMBO-0331256-273908	03 ^h 31 ^m 25 ^s .612	-27°39′08″.48	23.209 ± 0.021	24.418 ± 0.070	ext., SN candidate
33	COMBO-0333211-273912	03 ^h 33 ^m 21 ^s .077	-27°39′11″.90	20.151 ± 0.004	20.334 ± 0.006	
34	COMBO-0333037-273611	03 ^h 33 ^m 03 ^s .723	-27°36′10″.93	20.236 ± 0.003	20.369 ± 0.005	
35	COMBO-0332443-273403	03 ^h 32 ^m 44 ^s .274	-27°34′03″.37	22.201 ± 0.008	21.966 ± 0.008	

of $R \sim 22.5$ the significance criterion becomes stronger than the absolute threshold, thereby reducing the numbers again.

We show the location of the variables in a $(B - V)$ vs. $(V - R)$ color diagram in Fig. 10. The red magnitude is here only taken from October 1999 images to keep the color indices free from being skewed by long-term variability. The October frames have been taken during 9 days, so short-term variability could still have changed the color indices, especially for RR Lyrae stars given their typical periods of ~ 1 day. Also shown are expected colors for stars from the Pickles atlas (compare with Fig. 8) and for a quasar color library (Wolf et al. 2001) derived from quasar spectra modelled for $z = 0 \dots 6$ as a combination of power-law spectra, an emission-line contour (Francis et al. 1991) and Lyman-forest.

If we assume an absence of short-term variability, we would classify most objects as quasars or Seyfert galaxies, while some could be stars. Of course, the stellar sample could contain some

RR Lyrae stars whose variability time scale of ~ 1 day could offset their colors. These color offsets could move the stars in any directions (+/-) along any of the color axes with equal probability, and a scattered sample should appear with a comparable fraction of stars below and above the original color sequence.

In Fig. 10 we see that only three objects show up below the stellar sequence, while ~ 30 are located above. Therefore we conclude that most of the variable objects presented are indeed quasars. RR Lyrae stars in this sample of variables would typically have $V = 20.5 \dots 23.5$. Given their average absolute magnitude of $M_V \approx 0.5$, they would reside at distances ranging from 100 kpc to 400 kpc. While the existence of such stars is not at all ruled out, the probability of finding faint quasars is significantly higher.

The bulk of rather blue variables having $B - V < 0.3$ and $V - R < 0.5$ would then be quasars at $z < 3$, while the two red variable objects with $V - R \approx 0.7$ and $B - V < 0.25$ are

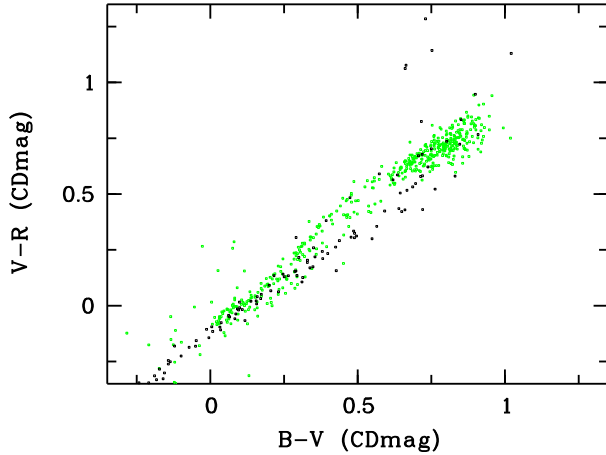


Fig. 8. $B - V$ and $V - R$ colors of observed stars in comparison with colors expected from synthetic photometry. Shown are stellar objects with $R = 17 \dots 21$ from the object catalog (grey dots) and the stars from the Pickles (1998) spectral library (black dots). We note, that most stars observed in our field belong to the halo population, while most stars in the Pickles library are nearby stars from the disk population. The populations form two arms that are clearly separated for G and K stars ($B - V \approx 0.3 \dots 0.6$). We also note a number of blue objects off the main sequence, which are probably quasars passing our purely morphological selection. The units of the colors are photon count color indices (CDmag) as introduced in Wolf et al. (2001), see also text.

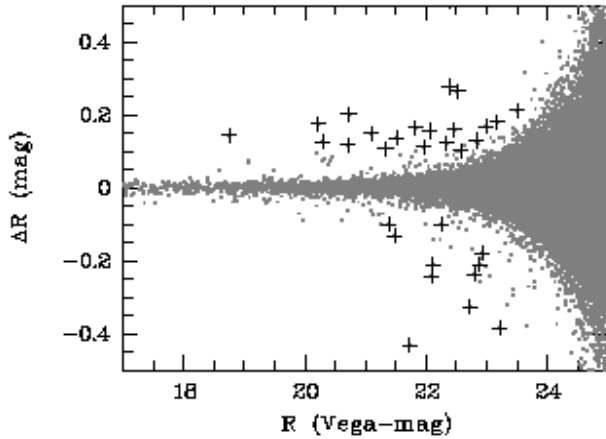


Fig. 9. R -band magnitude difference between the two epochs October 1999 and February 2000 versus combined R -magnitude (grey dots = all objects). Objects selected as variable are shown as black crosses, but strongly variable sources lie outside the plot. Twenty objects have been omitted from the sample after visual inspection since they were affected by scattered light or diffraction spikes of 9^{th} magnitude stars.

consistent with quasars at $z = 3.8 \dots 4.1$. But before we can derive final classifications here, we need more spectral bands. Some of the variable quasar candidates listed here are slightly extended, which applies in particular to one of the two $z \approx 4$ -candidates. These objects might actually be low-luminosity Seyfert-I galaxies where we resolved the host galaxy. The col-

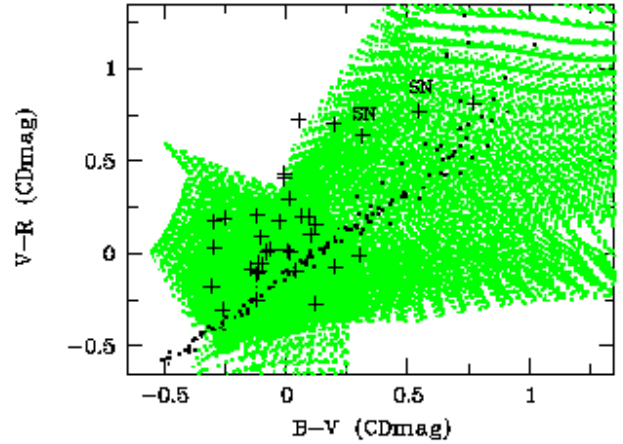


Fig. 10. Color-color diagram of variable objects (black crosses) compared with the expected stellar sequence (black dots) and a quasar color library (grey dots). Assuming the absence of short-term variability, most objects would be quasars, but few could as well be stars. Only one of these objects is brighter than $R = 20$. Two Supernova (SN) candidates are within the limits of this diagram.

ors could then be dominated by the host galaxy spectrum suggesting a much lower redshift, while the variability would result from the active nucleus.

Among the variable objects are also three candidates for Supernovae (see Table 5), which had their bright phase in October 1999 and are undetectable to visual inspection in the February coadded frame. Each of the first two showed up as a significant off-center brightening of a tiny faint galaxy (objects 9 and 32 in Table 5).

The third candidate has a rather red $B - V$ color (object 19 in Tab. 5). It is a point source located only $2''.0$ North and $0''.9$ East of a small galaxy with $R = 22.87 \pm 0.01$ appearing with an FWHM size of $2''.26 \times 1''.41$ in $0''.75$ seeing. There is still non-zero flux measured at the location of the transient object in February 2000 yielding $R = 25.33 \pm 0.19$, but it is not clear, whether the light originates from the outskirts of the neighboring galaxy or still from the Supernova.

In October it was measured on Oct 10 with $V = 23.72 \pm 0.05$, on Oct 13 with $B = 25.50 \pm 0.17$ and on Oct 19 and 20 consistently with $R = 23.26 \pm 0.02$. Again, we can not decide on the B band sum frame with $1''.2$ PSF whether the B flux is contributed from the galaxy or from the candidate. If it was a Supernova, the B measurement bracketed by V and R imaging could not be explained by variability. Therefore, the object must be unusually red with $B - V \gtrsim 1.8$ and it is not entirely clear whether the Supernova hypothesis is the right explanation.

We note, that the Supernova 1999gu reported by Cappellaro et al. (2000) at $\alpha_{J2000} = 3^{\text{h}}33^{\text{m}}00^{\text{s}}.1$ and $\delta_{J2000} = -27^{\circ}51'40''$ in a galaxy at $z = 0.147$ is clearly visible in the images of February 2000 with $R = 21.5$, but since our master list was defined on the deep sum frame of October 1999, it is not contained in the catalog presented here.

5. Summary and Outlook

We have presented an overview of the COMBO-17 survey (*Classifying Objects by Medium-Band Observations in 17 filters*), where we included a detailed explanation of our data reduction process including astrometry and photometry. We have constructed a catalog with positions, morphology and deep *R*-band photometry ($R \lesssim 26$) of 63501 objects on an area of $31'5 \times 30'$ containing the Chandra Deep Field South. This catalog is available to the scientific public at Centre de Données astronomiques de Strasbourg (CDS, <http://cdsweb.u-strasbg.fr/>), and potentially very useful for the identification of X-ray sources. We have presented a first list of faint variable objects, which are supposedly mostly quasars. Three transient sources are suggestive of supernovae, but one of them had an unusually red color of $B - V \gtrsim 1.8$.

When fully reduced, the dataset collected by the COMBO-17 survey will provide a bonanza of pseudo-spectroscopic information. We expect to classify some 50 000 objects over an area of 1 deg^2 down to $I \lesssim 23$ (completeness limit). Besides the classification information (star, galaxy or quasar) we will get spectral subclasses and high-quality redshift estimates for extragalactic sources. The full catalog will then allow to finally classify also the variable sources and tell the redshifts of the Supernova host galaxies. It will not only provide an optical classification of the X-ray sources but also of neighboring objects in their environment.

Acknowledgements. The authors thank Hermann-Josef Röser for providing software macros for the astrometric reduction. This work was supported by the DFG (Sonderforschungsbereich 439).

References

- Baade, D., Meisenheimer, K., Iwert, O., et al., 1998, *The Messenger*, 93, 13-15
- Baade, D., Meisenheimer, K., Iwert, O., et al., 1999, *The Messenger*, 95, 15-17
- Baade, D., 1999, ESO WFI User Manual, p. 21, Doc. No. LSO-MAN-ESO-22100-00001
- Bertin, E., Arnouts, S., 1996, *A&AS*, 117, 393
- Bohlin R., Lindler D., 1992, *STScI Newsletter*, Vol. 9, No. 2, 19
- Cappellaro, E., et al., 2000, *IAU Circ.* 7346
- Francis, P. J., Hewett, P. C., Foltz, C. B., Chaffee, F. H., Weymann, R. J., Morris, S. L., 1991, *ApJ*, 373, 465
- Giacconi, R., et al., 2000, AAS HEAD meeting, 32, 07.01
- Pickles, A. J., 1998, *PASP*, 110, 863
- Röser, S., Bastian, U., 1991, *PPM Star Catalogue*, Spektrum Akademischer Verlag, Heidelberg
- Röser, H.-J., Meisenheimer, K., 1991, *A&A*, 252, 458
- Schlegel, D. J., Finkenbeiner, D. P., Davies, M., 1998, *ApJ*, 500, 525
- Wackermann, R., Diploma thesis, Universität Heidelberg, 1999
- Wisotzki L., Christlieb N., Bade N., Beckmann V., Köhler T., Vanelle C., Reimers D., 2000, *A&A* 358, 77
- Wolf, C., Meisenheimer, K., Röser, H.-J., 2001, *A&A*, in print
- Wolf, C., Meisenheimer, K., Röser, H.-J., Beckwith, S. V. W., Chaffee, Jr., F. H., Fried, J., Hippelein, H., Huang, J.-S., Kümmel, M., v. Kuhlmann, B., Maier, C., Phleps, S., Rix, H.-W., Thommes, E., Thompson, D., 2001, *A&A*, in print